Stabilizing Anionic Redox Chemistry in a Mn-Based Layered Oxide Cathode Constructed by Li-Deficient Pristine State

Xin Cao, Haifeng Li, Yu Qiao,* Min Jia, Xiang Li, Jordi Cabana and Haoshen Zhou*

X. Cao, Dr. Y. Qiao, M. Jia, Prof. H. Zhou

Energy Technology Research Institute, National Institute of Advanced Industrial Science and Technology (AIST), 1-1-1, Umezono, Tsukuba 305-8568, Japan.

E-mail: kyou.qiaoyu09206@aist.go.jp (Y. Q.); hs.zhou@aist.go.jp (H. Z.)

H. Li, Prof. J. Cabana

Department of Chemistry, University of Illinois at Chicago, Chicago, Illinois 60607, United States

Prof. H. Zhou

Center of Energy Storage Materials & Technology, College of Engineering and Applied Sciences, Jiangsu Key Laboratory of Artificial Functional Materials, National Laboratory of Solid State Microstructures, and Collaborative Innovation Center of Advanced Microstructures, Nanjing University, Nanjing 210093, P. R. China E-mail: hszhou@nju.edu.cn (H. Z.)

X. Cao, M. Jia, Prof. H. Zhou

Graduate School of System and Information Engineering, University of Tsukuba, 1-1-1, Tennoudai, Tsukuba 305-8573, Japan

Dr. Xiang Li

Argonne National Laboratory, 9700 S. Cass Avenue, Lemont, IL 60439, United States

§ X. C. and H. L. contributed equally to this work.

Keywords: lithium-ion batteries, cathode materials, anionic redox reactions, oxygen release, structure distortion

Abstract

Li-rich cathode materials are of significant interest for coupling anionic redox with cationic redox chemistry to achieve high-energy-density batteries. However, lattice oxygen loss and derived structure distortion would induce serious capacity loss and voltage decay, further hindering its practical application. Herein, we developed a novel Li-rich cathode material, O3-type Li_{0.6}[Li_{0.2}Mn_{0.8}]O₂, with the pristine state displaying both a Li excess in the transition metal layer and a deficiency in the alkali metal layer. Benefiting from stable structure evolution and reversible Li migration, not only can high reversible capacity (~329 mAh g⁻¹) be harvested but also anionic/cationic redox chemistry has been comprehensively quantified via the combination of in/ex-situ spectroscopies. Furthermore, irreversible lattice oxygen loss and structure distortion have been effectively restrained, resulting in long-term cycle stability (capacity drop of 0.045% per cycle, 500 cycles). Altogether, tuning the Li state in alkali metal layer presents a promising way for modification of high-capacity Li-rich cathode candidates.

To fulfill the requirement of energy storage systems in next decade, a great improvement of energy density would be achieved by introducing attractive oxygen redox chemistry in existing battery systems.^[1] Li-rich cathode materials are widely considered as promissing candidates since oxygen redox activities can be triggered to provide extra capacities, which is limited to conventional transition metal (TM) redox reactions.^[2] However, pernicious capacity loss and operating voltage decay seriously hinder the further development of practical application.^[3]

The irreversible lattice oxygen loss and derived structure distortion (layered structure to spinel phase) are intrinsical reasons for the degradation of structural stability and electrochemical reversibility in Li-rich layered oxides. [4] Especially, lattice oxygen release within typical Li-rich materials is severe during the initial charging process. [5] As a result, it would induce that the capacities triggered by first deep oxygen activation process cannot be reversibly utilized during anionic reduction process since the complete extraction of Li₂O from bulk materials. [6] What's worse, the gaseous oxygen release inevitably triggers deleterious structure distortion induced by TM migration, resulting in continuous operating voltage decay during long-term cycling. [3d, 3e, 7] To address these issues, on the one hand, substitution with 4d/5d metals can stabilize the anionic redox activities by strengthening hybridization of O 2p orbitals and metal orbitals. [8] On the other hand, surface modifications such as coating and doping have been demonstrated as an effective way to enhance structural stability, further suppressing lattice oxygen release during Li⁺ deintercalation. [9]

Therefore, it is crucial to develope more modification methods based on the view of restraining irreversible oxygen behaviors during the pristine oxygen activation process. Moreover, owing to lack of comprehensive assignment/quantification analyses on irreversible/reversible oxygen redox behaviors, the overlap regions of redox centers present on galvanostatic electrochemical curves further puzzle the clarification of intrinsic charge compensation mechanism of anionic/cationic redox chemistry.^[10]

In this study, we developed a novel Li-rich Ni/Co-free O3-type Li_{0.6}[Li_{0.2}Mn_{0.8}]O₂ cathode material by a facile ion-exchange method from Na-precursor P3-type Na_{0.6}[Li_{0.2}Mn_{0.8}]O₂ with reversible anionic redox behaviors. Unlike other typical O3-based Li-rich layered cathodes, the alkali metal layer presents Li-deficient state. Benefitting on comprehensive spectroscopy characterization, anionic oxygen and cationic Mn redox reactions are assigned and quantified, demonstrating both lattice oxygen release and structure distortion are effectively restrained. As a result, high reversible capacity (~329 mAh g⁻¹) and excellent long-term cycle stability (capacity drop of 0.045% per cycle, 500 cycles) have been successfully achieved owing to stable structure evolution and reversible Li migration during cycling.

O3-type $Li_{0.6}[Li_{0.2}Mn_{0.8}]O_2$ (defined as LMO) was synthesized through facile ion exchange method from $Na_{0.6}[Li_{0.2}Mn_{0.8}]O_2$.^[11] The Na-deficient precursor is a typical P3-type cathode material with Li/Mn in TM layer, as verified by Rietveld refinement of its XRD pattern (Figure S1 and Table S1) and elemental analysis by inductively

coupled plasma (ICP, Table S2). The structural and electrochemical characterizations of Na-based precursor were also investigated (Figures S2 and S3). After ion-exchange, the as-prepared LMO was characterized by XRD measurement and the corresponding Rietveld refinement results were calculated by General Structure Analysis System (Figure 1a and Table S3) with goodness-of-fitting parameters of χ^2 (2.48) and R_{wp} (7.4%). The peaks shown in the calculated patterns fit well with the experimental result, which can be well indexed with a trigonal O3-type arrangement

with the space group $R\overline{3}m$. The calculated lattice parameters of LMO are a=b=2.84(6) Å, c=14.42(5) Å, $\alpha=\beta=90^{\circ}$, $\gamma=120^{\circ}$. Besides, the chemical formula of LMO was also confirmed by ICP (Table S4), indicating sodium ions within the alkali metal layer are replaced by lithium ions from the molten salt. Moreover, based on field emission scanning electron microscope (FESEM, Figure S4) and high resolution transmission electron microscopy (HRTEM, Figure 1a, insert) images, the LMO displayed a morphology of nanosheets inherited from its precursor with large diameter distribution from 50 to 300 nm where the interlayer spacing of 0.48 nm fits well with the (003) plane.

The electrochemical performance of LMO as cathode material was evaluated by galvanostatic cycling, delivering high capacity of 197 mAh g⁻¹ in the high-voltage plateau region upon initial charge (Figure 1b). These capacities correspond to 0.6 mol Li extracted from LMO, and can be hypothetically attributed to a process purely centered at the oxygen ligands since the Mn⁴⁺ cannot be further oxidized in layered

oxides, which will be proved by following valence state assignments.^[12] During subsequent discharging to 2 V, additional Li inserted into the layered structure with the final formal composition of Li_{1.13}Mn_{0.8}O₂, displaying a typcial "S-shape" discharge curve like most Li-rich Mn-based cathode materials, which is typically explained as Mn reducation processes participate in Li⁺ intercalation process at lower voltage.^[13] Unlike the initial charge, two plateaus occurred at around 3.0 V and 4.5 V during the second charge, which might correspond to two electrochemical reations, conventional cationic oxidation of Mn³⁺ to Mn⁴⁺ and oxygen-related oxidation of lattice oxygen to peroxo, superoxo species and even to gaseous oxygen states at high voltage, respectively. More intriguingly, reverisible discharge capacity of 329 mAh g⁻¹ (~1.0 Li⁺ insertion, final composition of Li_{1.2}Mn_{0.8}O₂) and high energy density of 1100 Wh/kg can be achieved during second Li⁺ intercalation. Furthermore, excellent cycling and rate performance can be achieved with LMO. A capacity of 281 mAh g⁻¹ can be delivered after 20 cycles at 10 mA/g (Figure 1b, insert) and the cathode harvests exceptional capacity rentention (211 mAh g⁻¹) at 200 mA/g (Figure S5). Even expanding current density to 300 mA g⁻¹ (Figure 1c), limited capacity decay (average capacity drop of 0.045 % upon 500 cycles) can be achieved, which indicates stable anionic/cationic redox processes, favorable kinetics and excellent structure stability within LMO during long-term cycling.

To investigate the variation of the electonic structure of O upon Li (de)intercalation, O K-edge X-ray absorption spectroscopy (XAS) spectra were collected under both total electron yield (TEY, probe depth of ~10 nm, surface

sensitive) mode and total fluorescence yield (TFY, probe depth of ~100 nm, bulk information) mode. O K-edge XAS could be employed to investigate the variation of the electonic structre of O upon Li (de)intercalation, demonstrating a pre-edge region (below 535 eV), arising from the transition to the unoccupied states of O 2p orbitals hybridized with Mn 3d orbitals, and a broad band (above 535 eV), derived from from the transition from O 1s to empty O 2p hybridized with Mn 4s/4p orbitals, followed by higher states and multiple scattering events of the ejected electrons. The two peaks in the pre-edge regin of the pristine state with the gravematric center at around 529.3 and 531.9 eV are ascribed to the transtion to the t_{2g} and e_{g} states, respectively (Figure 2a). The first oxidation to 4.8 V led to a slight reduction in the peak intensity and only shifted the eg peak to lower energy by 0.3 eV and preserved the position of t2g peak and the absorption threshold, consitent with Mn^{3+/4+} oxidation in the surface. Upon the subsequent discharge to 2.0 V, a large Li insertion resulted into a substantial reduction in the peak intensity and a higher energy shift of t_{2g} peak by 0.4 eV and little energy shift for eg peak and a shift of the absorption threshold to lower energy shift by 1.1 eV, which is in good agreement with the reduction process and the existence of mixed Mn²⁺ and Mn³⁺ from Mn L-edge TEY XAS spectra as previously reported.^[14] The peak at 533.3 eV is attributable to the presence of impurities such as Li₂CO₃. The second charge to 4.8 V recovered the absorption threshold postion and the pre-edge part but with a relatively lesser intensity and higher eg position than the first charged state, consitent with Mn oxidation and the coexistence of Mn³⁺/Mn⁴⁺ at the surface. Upon the second reduction to 2.0 V, the spectral shape was similar to the first

discharge state but with a marginal energy shift for t_{2g} and e_g peaks and the absorption threshold higher energy shift for t_{2g} peak (by 0.2 eV) and t_{2g} peak (by 0.3 eV) and the absorption threshold (0.5 eV) as well as a slight increase in the peak intensity, well agreeing with the Mn-based reduction processes.

In contrast to TEY spectra, TFY spectra displayed different behaviror of O during cycling (Figure 2b). Upon charging to 4.8 V, the large Li removal gave rise to little change in the peak position and intensity for t2g and eg peaks and the absorption threshold, but led to a shoulder feature at ~530. 5 eV probably due to the occurrence of the unoccupied O state accounting for the Li removal, in relative to the pristine state. The subsequent reduction to 2.0 V substantially reduced the intensity of both pre-edge peaks with much lower than the pristine state, reflecting a large decrease in the unoccupied states, and greatly shifted the absorption threshold to lower energy, implying a augment in the effective nuclear charge Zeff. The subsequent oxidation to 4.8 V almost restored the pre-edge part and the absorption threshold to the first charge state, strongly reflecting the reversibility of the oxygen electronic structure with cycling. The second reduction to 2.0 V resulted in similar variations to the first reduction state, but with a little higher energy shift of pre-edge peaks and the absorption outset, as well as a slight larger intensity of the pre-edge peaks, again reflecting a reversible electrochemical process after the first charge.

Mn L-edge XAS were also collected to investigate the variation of Mn chemical states. The signals originate from the electron transition from Mn 2p orbitals to unfilled Mn 3d orbitals. Compared with the reference spectra of MnO₂ (+4), Mn₂O₃

(+3) and MnO (+2), Mn in the pristine state is the mixture of dominant Mn⁴⁺ and negligible Mn³⁺ on the surface, as expected (Figure 2c).^[15] Compared to the TEY spectra, the features in the Mn L₃-edge TFY XAS were significally washed out due to self-absorption (Figure 2d). Comparison of the position of the L₂-edge with reference data revealed that Mn in the bulk of the pristine state was Mn⁴⁺. Upon the first oxidation to 4.8 V, apparently there was no shift for L₂-edge feature, indicating Mn was not involved in the charge compensation associated with the Li removal. Thus, it is rational to deduce that pure oxygen-related anionic reactions are mainly responsible for the capacity of 197 mAh/g. The subsequent reduction to 2.0 V shifted the L₂-edge peak to lower energy than the pristine state, reflecting the reduction to Mn³⁺ with Li insertion. The L₂-edge peak underwent a similar variation upon the second charge and discharge process to the first cycling process, suggesting a reversible evolution of the Mn electronic structure coupled with Li (de)intercalation. The comparison of Mn L-edge spectra between TEY and TFY unambiguous demonstrated a distinct behavior of Mn between the surfacial and internal material: the surficial Mn experienced more reduction with respect to the interior Mn upon reduction while both was oxidized to Mn⁴⁺.To better evaluate the capacity contributions in LMO upon cycling, TFY Mn L-edge XAS of LMO at different states, MnO₂ and Mn₂O₃ are employed to quantify the Mn³⁺/Mn⁴⁺ redox reactions during Li⁺ (de)intercalation processes (Figure 2e). For instance, the ratio of Mn³⁺ (58 %) and Mn⁴⁺ (42 %) in first discharged LMO can be calculated by peak area calibration, futher deducing that the cationic capacity contribution of reducation reaction of partial Mn⁴⁺ to Mn³⁺ is 141.8 mAh/g. Moreover, the Mn³⁺/Mn⁴⁺ ratio and corresponding capacity contributions of Mn-based redox reactions at different states are summarized by the same method (Figure 2f).^[16] It is significant to quantify capacity attributions of irreversible and reversible anionic oxygen-related redox reactions and further unravel the underlying mechanisms of oxygen redox chemistry.

Further in-depth probing of reversible/irreversible oxygen-related redox behaviors within LMO are identified and quantified by the combination of operando differential electrochemical mass spectrometry (DEMS) and in-situ Raman spectroscopy (Figure 3a).^[5] These two techniques are generally recognized as effective methods to accurately characterize oxygen-related speices (especially for peroxo/superoxo species and O2), which is beneficial to systematically unravel the underlying mechanisms of reversible/irreversible anionic redox reactions. In the first place, an obvious reversible trendency can be detected in peroxo O-O stretch region (795 ~ 845 cm⁻¹) both in first and second cycles, indicating that lattice oxygen can be oxidized to peroxo speices during charging and reversibly reduced back to initial state after discharging. Moreover, compared with the first cycle, the peak of peroxo O-O stretch in second cycle exhibits higher intensity and broader area in this region shown in corresponding color mapping, indicating more reversible capacities are triggered by oxidation of lattice oxygen to peroxo species upon second charging. Furthermore, shorter O-O distance (around 833 cm⁻¹) obtained at first charged state also demonstrates more moderate oxygen-related oxidation reactions than second charging with larger O-O distance (around 824 cm⁻¹). It is because the serious reduction of O-O distance would inevitably lead to harmful polarization, further resulting in the irreversible oxygen behaviors (the formation of superoxo species and/or gasous O₂). Therefore, at the end of initial charge process, a sharp peak appeared at 1104 cm⁻¹ can be assigned to the formation of superoxo species, while this parasitic product then quickly disappeared once formed. More serious, with the further shrink of O-O distance, superoxo species are further oxidized to O₂ (254 µmol/g) at the final end stage of the initial charging, which can be identified and quantified by DEMS. Besides, superoxo-induced nucleophilic reaction attacking towards PC electrolyte would cause the formation of Li₂CO₃ (around 1105 cm⁻¹) on surface, which is also demonstrated by TEY O K-edge XAS results. During the subsequent cycles, the decomposition of carbonates would further lead to the evolution of CO₂ (47 µmol/g) in high-voltage region, which is precisely detected and quantified by operando DEMS. Notably, the irreversible oxygen loss (O₂-/O₂) can not be detected anymore, which further illustrates the reversibility of anionic redox reactions. All together, the combination of operando Raman spectroscopy and DEMS further support the existence of a reversible process centered at the lattice oxygen, which is consistent with the changes of O electronic structures obtained by XAS.

Typically, the O₂ originates from the further oxidization of peroxo/superoxo species but cannot be assigned to carbonate oxidation nor electrolyte degradation. Based on the 4e⁻ oxidation process of lattice 2O²⁻ to O₂, the irreversible capacity contribution of O₂ gas formation (254 μmol/g, total amount) can be evolved as 27.2 mAh/g. Moreover, the capcaity contribution of CO₂ evolution and Li₂CO₃ deposition

also can be calculated, delivering limited capacity of around 7.1 mAh/g predominantly originated form continuous PC degradation. Therefore, the pristine active material loses 2.5 % (0.05 mol in chemical formula) of the total lattice oxygen during the first charge. Consequently, combined with quantitative DEMS and XAS mesurement, capacity contributions of anionic oxygen redox and cationic Mn redox reactions can be obtained (Figure 3b, top). Interestingly, it is worth mentioning that a substantial proportion of total capacities are contributed by reversible oxygen redox reactions upon inital two cycles, delivering 53.3 % and 57.4 % of total capacities during first and second discharge processes, respectively. Thus, more reversible oxygen redox capacity can be triggered during second cycle, which is consistent with the higher reversible oxygen-related signals obtained from TFY O K-edge XAS and Raman results.

Through comprehensive spectroscopic analysis, the underlying mechanisms of reversible/irreversible anionic redox reactions are systematically proposed (Figure 3b, bottom). Firstly, reversible anionic redox reactions between lattice oxygen and peroxo species can be achieved, where the O2p σ^* orbital hybridizes with the Mn 3d orbital to lie above the Fermi level with fully occupied π^* , π and σ orbitals. Then, along with Fermi level decreasing, the valence electron is depleted from π^* orbital, resulting in the formation of superoxo species (partial occupied π^* orbital state). As the valence electrons are successively removed from π^* orbital, gaseous O2 releases from lattice oxygen network with the formation π bond (half occupied π^* orbital state). These over-oxidized products (irreversible superoxides and oxygen loss) would reduce the

covalency of Mn–O to Mn⁴⁺, further resulting in rearrangement of oxygen network and destructive TM migration, which should be restrained and suppressed during deintercalation process. In our LMO, the depletion of π^* electron and the formation of O_2^-/O_2 only exists in the initial charging but reversible oxygen redox reactions occur during subsequent cycles.

Operando XRD measurements were conducted to evaluate the reversibility of structural evolution of LMO upon the initial two Li⁺ delithiation/lithiation processes (Figure 4a and S6). During initial charging, the (003) peak obviously shifted to higher angle while the (101) peak have slight shifting, which is contrary with Li⁺ deintercalation processes of conventional cationic redox reactions, indicating this process is associated with oxygen-related anionic oxidation alongside the c-lattice collapse. Moreover, the structural evolution process during the second charge presents reverse process with the first discharge and then the second discharge process displays similar structural evolution relative to the initial discharge. Besides, the XRD patterns of corresponding three LMO electrodes after 1, 20 and 50 cycles deliver no obvious structure distortion, all representing trigonal O3-type arrangement with the space group Rm, which indicates the LMO electrode keeps well structural stability during long-term cycling (Figure S7 and Table S5-S7).

In order to further investigate the relationship between structure stability and reversibility of oxygen redox, ⁷Li solid state nuclear magnetic resonance (ssNMR) spectroscopy was employed to monitor Li migration and identify different local environments at lithium (de)intercalated states (Figure 4b).^[17] The resonances at

1300~1650 ppm can be assigned to Li sites within the TM layers, while the resonance at 500~1000 ppm is attributed to Li in the alkali metal (AM) layer. At charged (Li-deintercalated) state, about 0.2 mol Li resides in AM layers while 0.6 mol Li TM layer was removed out of the lattice, deliverig the coexistence of Vac-O-Li and Vac-O-Vac configurations in Li_{0.2}Mn_{0.8}O₂. After discharge to 2 V, according to results of peaks area fitting, the crystallographic site occupancy of Li in AM layer increases to 85 % with two local environments arranged by Li–O–Li (16 %, 0.18 mol) and Li-O-Mn configurations (69 %, 0.78 mol). Notably, Li in AM layer also increased to 15 % (0.17 mol), indicating the reversible migration of Li between TM and AM layer, which provides solid foundation of reversible (de)intercalation processes within LMO during long cycling. Furthermore, the influence of phase transition was further revealed by the comparison between our LMO and cannonical prototype of Li-rich material Li₂MnO₃ (Li[Li_{0.33}Mn_{0.67}]O₂) (Figure 4c). After 20 cycles, the capacity-normalized Li₂MnO₃ exhibits serious discharge voltage decay than current Li_{0.6}[Li_{0.2}Mn_{0.8}]O₂ cathode on galvanostatic discharge profiles. The voltage decay of Li₂MnO₃ is generally considered to stem from an increased spinel phase (cubic) content. The suppressed voltage decay within LMO implies that the layered to spinel phase transition has been effectively restrained, which is verified by the ex-situ Raman spectra collected from corresponding cycled electrodes. Sharing the similar Li-rich construction in TM layer, we propose that the differnce on structure distortion between typical Li-rich materials (Li-stuffed state) and current LMO (Li-deficient state) can be ascribled to the difference of pristine state in alkali metal layer.

The two-component notation is employed to dictate the structure evolution and electrochemical properties of Li-rich xLi₂MnO₃·(1-x)LiMO₂ electrodes during charge and discharge. [6] Herein, we expand the classic Li₂MnO₃-LiMO₂-MO₂ compositional phase diagram to Li₂MnO₃-LiMO₂-MnO₃ configuration by introducing MnO₃ region, which can clearly present reversible (Li₂MnO₃–MnO₃ direction in left triangle, Li₂MnO₃-MnO₂-MnO₃) and irreversible (LiMnO₂-MnO₂ direction in right triangle, Li₂MnO₃-LiMnO₂-MnO₂) oxygen-related anionic redox reactions in these typical Li-rich compounds (Figure 4d). Furthermore, with the new notation, pure oxygen oxidation reactions occur in the LMO electrodes (blue trace) while typical Li-rich cathode (black trace) has concomitant oxidation processes of cationic transition metals during the initial lithium deintercalation process. Meanwhile, the LMO has only slight oxygen loss (0.05 mol) but Li-rich cathode (red trace) suffers serious irreverible oxygen loss. Subsequently, during lithium intercalation process, TM couples in Li-rich cathode are reduced to lower valence compared with the pristine state to compensate the capacity loss caused by harmful lattice oxygen loss (LiMnO₂-MnO₂ direction). Therefore, based on schematics of phase diagram, the route of ideal Li-rich materials can be concluded: (1) boosting the Li₂MnO₃-MnO₃ direction to trigger more capacities from oxygen redox reactions. (2) restraining the LiMnO₂-MnO₂ direction to reduce irreversible oxygen loss. Typically, started at A point, normal Li-rich materials trigger both cationic (blank line in yellow triangle region) and anionic (blank line in green triangle region) whereas serious lattice oxygen release (red line in green triangle region) can be detected. However, the pristine LMO presents as a novel Li-rich state in TM layer and Li-deficient state in AM layer, resulting the limited irreversible oxygen loss (0.05 mol O loss in formula) and higer cationic valence state than typical Li-rich cathode materials.

In this work, we developed a Ni/Co-free Li_{0.6}[Li_{0.2}Mn_{0.8}]O₂ as cathode material by modifying pristine Li content within TM and AM layer, in which the alkali metal layer presents a novel Li-deficient state. Benefitting from the nature of Li location within TM layer, LMO harvests high capacity of 197 mAh g⁻¹ triggered by anionic oxygen-related reactions upon frist charging, which possesses excellent retention (~189 mAh/g) during subsequent discharging process. Furthermore, combined with reversible Mn-based redox activities, a high discharge capacity and energy density (~329 mAh $g^{-1},~\sim\!1100$ Wh/kg) can be achieved. By constructing systematic in/ex-situ spectroscopic characterization system (in-situ Raman/DEMS/XRD, ex-situ XAS/Raman, etc.), not only the complicated Mn/O-related redox behaviors have been accurately quantified but also corresponding cationic/anionic redox reactions can be well assigned with dis/charge processes. Moreover, the stable structure evolution and reversible Li migration also can be clearly demonstrated by XRD and ssNMR, providing soild foundation of cationic/anionic redox chemistry in long term cycling. Altoghter, by successfully restraining the severe lattice oxygen release and voltage decay, modification towards Li content within alkali metal layer provides feasible means for designing better Li-rich materials to assess reversible cationic/anionic redox chemistry.

Acknowledgements

X.C. and H.L. contributed equally to this work. This research was partially supported and Development Program by the National Key Research of China (2016YFB0100203) and the National Natural Science Foundation of China (21633003, U1801251). H.L. and J.C. were supported by the National Science Foundation under Grant No. DMR-1809372. This research used resources of the Advanced Photon Source, a U.S. Department of Energy (DOE) Office of Science User Facility operated for the DOE Office of Science by Argonne National Laboratory under Contract No. DE-AC02-06CH11357. The authors thank Advanced Photon Source at Argonne National Laboratory. The authors thank Prof. Mineyuki Hattori (AIST, Japan) and Prof. Hayashi Shigenobu (AIST, Japan) for their help on solid NMR characterization and analysis. X.C. acknowledges the scholarship from the China Scholarship Council (CSC).

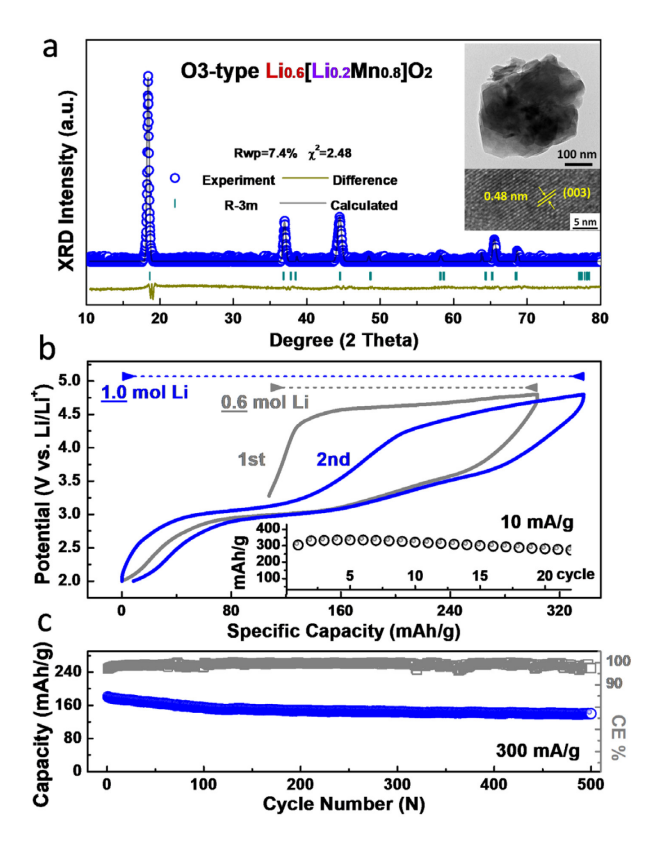


Figure 1. Structural characterization and electrochemical performance of O3-type LMO. (a) XRD patterns of LMO and the corresponding results of Rietveld refinement. The insert images are the corresponding TEM and HRTEM results. (b) Typical charge–discharge profiles of LMO between 2 and 4.8 V at the current density of 10 mA g^{-1} . The insert shows the corresponding discharge capacity retention. (c) Cycling performance of LMO between 2 and 4.8 V at the current density of 300 mA g^{-1} .

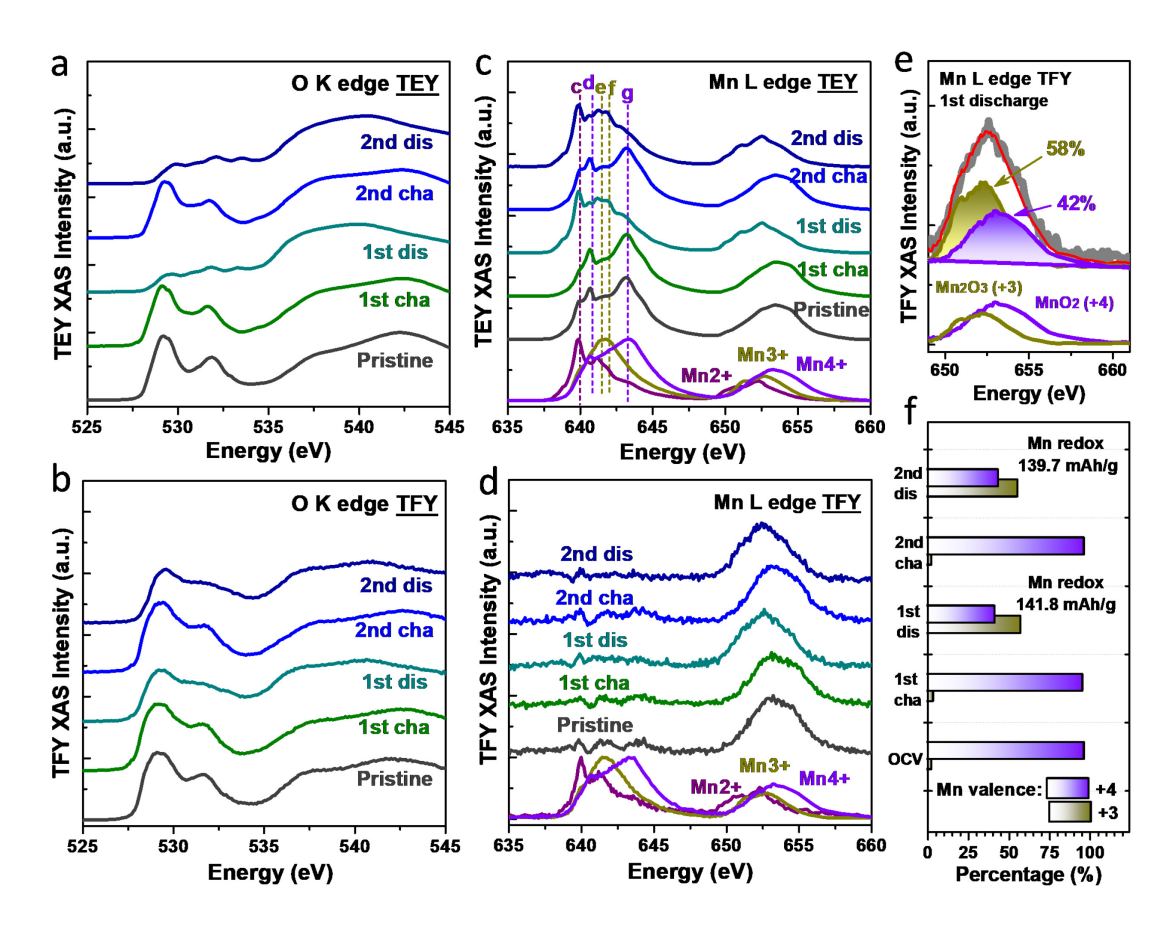


Figure 2. Anionic/cationic states analyses during initial two cycles. X-ray absorption spectra (XAS) of O K-edge XAS spectra, determined from (a) TEY mode and (b) TFY mode, of LMO at different states of charge. (c) Mn L_{2,3}-edge XAS spectra collected from (c) TEY mode and (d) TFY mode of LMO at different states of charge. Absorption events characteristic of Mn oxidation states of 2+ (c), 3+ (e and f), and 4+ (d and g) have been provided as a guide to the eye. Spectra are shown after multiple loss events and background has been subtracted. (e) TFY Mn L-edge XAS of 1st discharged LMO, MnO₂ and Mn₂O₃ to quantify the ratio of Mn³⁺ and Mn⁴⁺. The reference spectra of MnO₂ and Mn₂O₃ are collected at same condition and gain 0.5 times intensity for more accurate fitting and clear comparison. (f) Quantified Mn³⁺/Mn⁴⁺ ratio in LMO by fitting Mn L-edge XAS collected at TFY mode at different states.

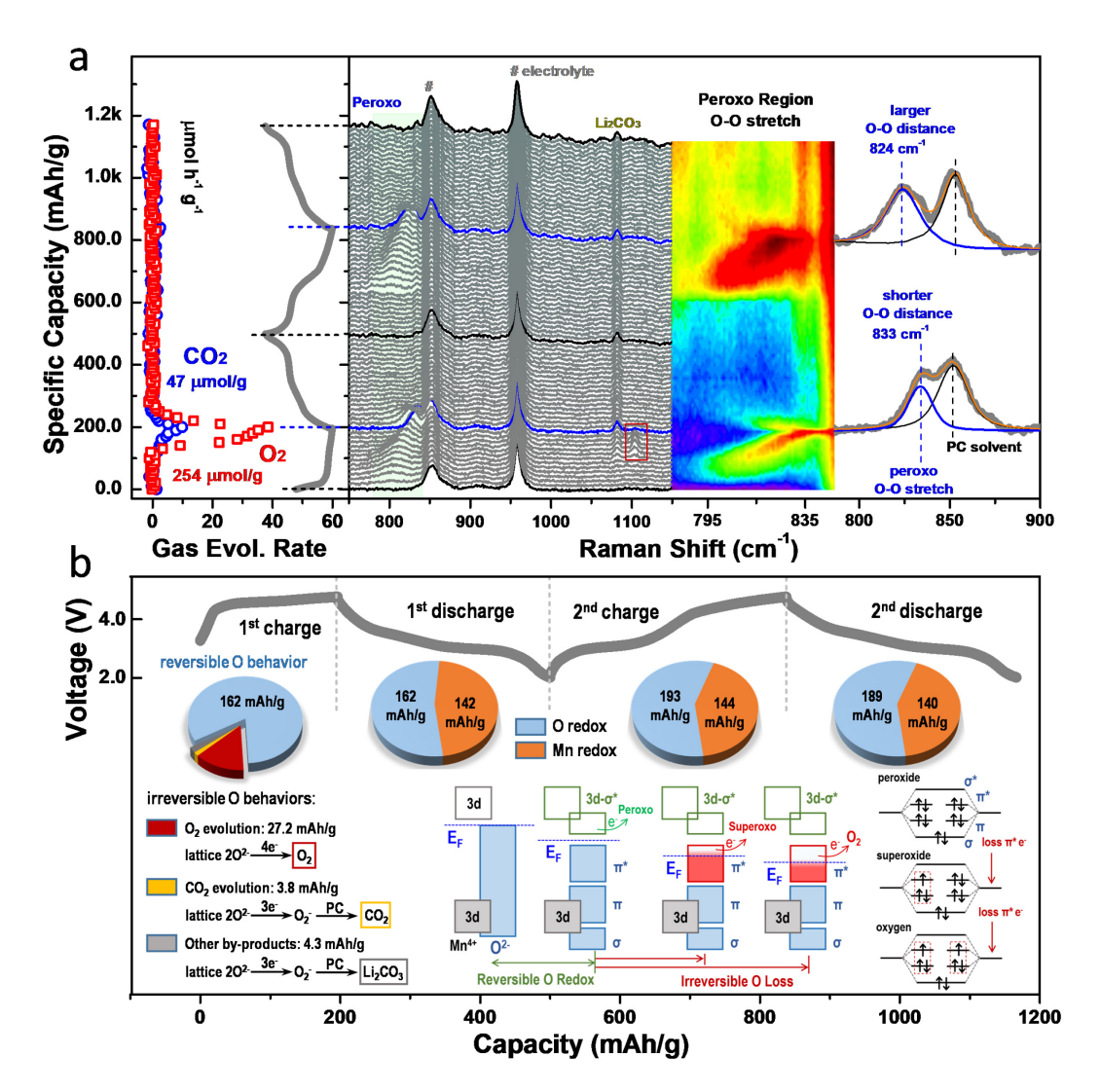


Figure 3. Additional insight into oxygen-centered processes. (a) operando differential electrochemical mass spectrometry (DEMS) of gas evolution rate and in-situ shell-isolated nanoparticle-enhanced Raman spectroscopy (SHINERS) during first and second cycles. (b) the capacity contributions of oxygen redox (reversible oxygen behavior, O₂ evolution, CO₂ evolution and others) during initial two cycles and the schematic diagram of oxygen redox mechanisms.

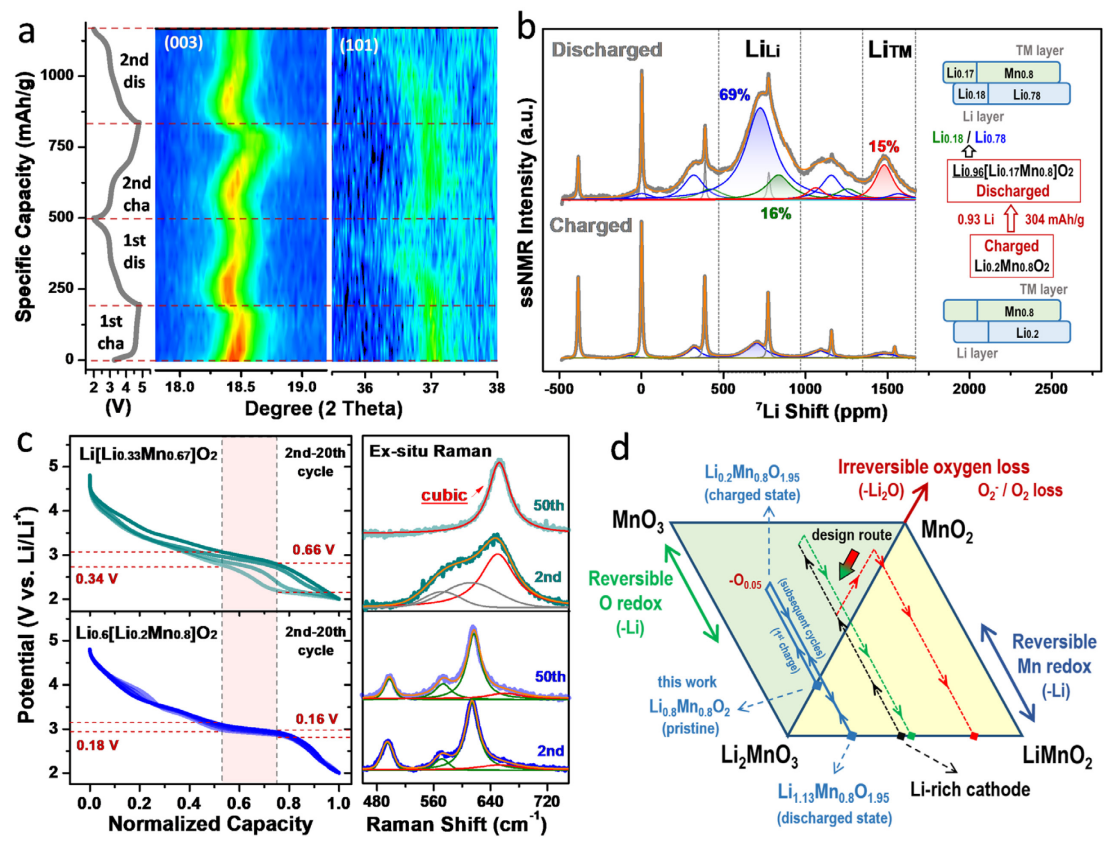


Figure 4. Structural and phase evolution processes of LMO during cycling. (a) operando XRD patterns of LMO electrode during the initial two cycles. (b) ⁷Li solid state NMR spectra of LMO electrode samples after initial charge to 4.8 V and initial discharge to 2 V. (c) the 2nd-20th discharge profiles of LMO and LiLi_{0.33}Mn_{0.67}O₂ and corresponding ex-situ Raman spectra of 2nd and 50th cycles at discharged states. (d) the compositional phase diagram showing the electrochemical reaction pathways for LMO electrode and typical Li-rich Mn-based cathodes.

References

- [1] a) R. Bi, N. Xu, H. Ren, N. Yang, Y. Sun, A. Cao, R. Yu, D. Wang, *Angew. Chem. Int. Ed.* **2020**, *59*, 4865-4868; b) M. Sathiya, G. Rousse, K. Ramesha, C. P. Laisa, H. Vezin, M. T. Sougrati, M. L. Doublet, D. Foix, D. Gonbeau, W. Walker, A. S. Prakash, M. Ben Hassine, L. Dupont, J. M. Tarascon, *Nat. Mater.* **2013**, *12*, 827-835; c) A. Grimaud, W. T. Hong, Y. Shao-Horn, J. M. Tarascon, *Nat. Mater.* **2016**, *15*, 121-126; d) E. Zhao, Q. Li, F. Meng, J. Liu, J. Wang, L. He, Z. Jiang, Q. Zhang, X. Yu, L. Gu, W. Yang, H. Li, F. Wang, X. Huang, *Angew. Chem. Int. Ed.* **2019**, *58*, 4323–4327.
- [2] a) H. Chen, M. S. Islam, *Chem. Mater.* **2016**, *28*, 6656-6663; b) W. E. Gent, K. Lim, Y. Liang, Q. Li, T. Barnes, S. J. Ahn, K. H. Stone, M. McIntire, J. Hong, J. H. Song, Y. Li, A. Mehta, S. Ermon, T. Tyliszczak, D. Kilcoyne, D. Vine, J. H. Park, S. K. Doo, M. F. Toney, W. Yang, D. Prendergast, W. C. Chueh, *Nat. Commun.* **2017**, *8*, 2091; c) B. Li, D. Xia, *Adv. Mater.* **2017**, 1701054.
- [3] a) A. Ito, D. Li, Y. Sato, M. Arao, M. Watanabe, M. Hatano, H. Horie, Y. Ohsawa, *J. Power Sources* **2010**, *195*, 567-573; b) J. R. Croy, H. Iddir, K. Gallagher, C. S. Johnson, R. Benedek, M. Balasubramanian, *Phys. Chem. Chem. Phys.* **2015**, *17*, 24382-24391; c) G. Assat, D. Foix, C. Delacourt, A. Iadecola, R. Dedryvère, J.-M. Tarascon, *Nat. Commun.* **2017**, *8*, 2219; d) K. Ku, J. Hong, H. Kim, H. Park, W. M. Seong, S. K. Jung, G. Yoon, K. Y. Park, H. Kim, K. Kang, *Adv. Energy Mater.* **2018**, *8*, 1800606; e) M. Sathiya, A. M. Abakumov, D. Foix, G. Rousse, K. Ramesha, M. Saubanere, M. L. Doublet, H. Vezin, C. P. Laisa, A. S. Prakash, D. Gonbeau, G. VanTendeloo, J. M. Tarascon, *Nat. Mater.* **2015**, *14*, 230-238.
- [4] a) X. D. Zhang, J. L. Shi, J. Y. Liang, Y. X. Yin, J. N. Zhang, X. Q. Yu, Y. G. Guo, *Adv. Mater.* **2018**, *30*, 1801751; b) E. Hu, X. Yu, R. Lin, X. Bi, J. Lu, S. Bak, K.-W. Nam, H. L. Xin, C. Jaye, D. A. Fischer, K. Amine, X.-Q. Yang, *Nat. Energy* **2018**, *3*, 619-620.
- [5]) J. Rana, J. K. Papp, Z. Lebens-Higgins, M. Zuba, L. A. Kaufman, A. Goel, R. Schmuch, M. Winter, M. S. Whittingham, W. Yang, B. D. McCloskey, L. F. J. Piper, *ACS Energy Letters* **2020**, *5*, 634-641.
- [6] M. M. Thackeray, S.-H. Kang, C. S. Johnson, J. T. Vaughey, R. Benedek, S. A. Hackney, *J. Mater. Chem.* **2007**, *17*, 3112.
- [7] D. Eum, B. Kim, S. J. Kim, H. Park, J. Wu, S. P. Cho, G. Yoon, M. H. Lee, S. K. Jung, W. Yang, W. M. Seong, K. Ku, O. Tamwattana, S. K. Park, I. Hwang, K. Kang, *Nat. Mater.* **2020**, *19*, 419–427.
- [8] a) X. Cao, H. Li, Y. Qiao, X. Li, M. Jia, J. Cabana, H. Zhou, *Adv. Energy Mater.* **2020**, 1903785; b) M. Saubanère, E. McCalla, J. M. Tarascon, M. L. Doublet, *Energy Environ. Sci.* **2016**, *9*, 984-991.
- [9] a) X. Ding, D. Luo, J. Cui, H. Xie, Q. Ren, Z. Lin, *Angew. Chem. Int. Ed.* **2020**, 59, 1-6; b) W. Zhang, Y. Sun, H. Deng, J. Ma, Y. Zeng, Z. Zhu, Z. Lv, H. Xia, X. Ge, S. Cao, Y. Xiao, S. Xi, Y. Du, A. Cao, X. Chen, *Adv. Mater.* **2020**, 2000496; c) R.-P. Qing, J.-L. Shi, D.-D. Xiao, X.-D. Zhang, Y.-X. Yin, Y.-B. Zhai, L. Gu, Y.-G. Guo, *Adv. Energy Mater.* **2016**, 6, 1501914; d) D. Kong, J. Hu, Z. Chen, K. Song, C. Li, M. Weng, M. Li, R. Wang, T. Liu, J. Liu, M. Zhang, Y. Xiao, F. Pan, *Adv. Energy Mater.* **2019**, 9, 1901756.

- [10]a) M. Ben Yahia, J. Vergnet, M. Saubanère, M.-L. Doublet, *Nat. Mater.* **2019**, *18*, 496–502; b) M. Oishi, K. Yamanaka, I. Watanabe, K. Shimoda, T. Matsunaga, H. Arai, Y. Ukyo, Y. Uchimoto, Z. Ogumi, T. Ohta, *J. Mater. Chem. A* **2016**, *4*, 9293-9302.
- [11] a) K. Du, J. Zhu, G. Hu, H. Gao, Y. Li, J. B. Goodenough, *Energy Environ. Sci.* **2016**, *9*, 2575-2577; b) J. R. D. J.M. Paulsen *Solid State Ion.* **1999**, *126* 3-24.
- [12] U. Maitra, R. A. House, J. W. Somerville, N. Tapia-Ruiz, J. G. Lozano, N. Guerrini, R. Hao, K. Luo, L. Jin, M. A. Pérez-Osorio, F. Massel, D. M. Pickup, S. Ramos, X. Lu, D. E. McNally, A. V. Chadwick, F. Giustino, T. Schmitt, L. C. Duda, M. R. Roberts, P. G. Bruce, *Nat. Chem.* **2018**, *10*, 288.
- [13] A. D. Robertson, P. G. Bruce, Chem. Mater. 2003, 15, 1984-1992.
- [14] B. Gilbert, B. H. Frazer, A. Belz, P. G. Conrad, K. H. Nealson, D. Haskel, J. C. Lang, G. Srajer, G. D. Stasio, *J. Phys. Chem. A* **2003**, *107*, ,2839-2847.
- [15] G. M. Nolis, A. Adil, H. D. Yoo, L. Hu, R. D. Bayliss, S. H. Lapidus, L. Berkland, P. J. Phillips, J. W. Freeland, C. Kim, R. F. Klie, J. Cabana, *J. Phys. Chem. C* **2018**, *122*, 4182-4188.
- [16] N. Li, S. Sallis, J. K. Papp, J. Wei, B. D. McCloskey, W. Yang, W. Tong, *ACS Energy Letters* **2019**, *4*, 2836-2842.
- [17]a) L. Yang, X. Li, J. Liu, S. Xiong, X. Ma, P. Liu, J. Bai, W. Xu, Y. Tang, Y. Y. Hu, M. Liu, H. Chen, *J. Am. Chem. Soc.* **2019**, *141*, 6680-6689; b) R. A. House, U. Maitra, M. A. Pérez-Osorio, J. G. Lozano, L. Jin, J. W. Somerville, L. C. Duda, A. Nag, A. Walters, K. Zhou, M. R. Roberts, P. G. Bruce, *Nature* **2019**, *577*, 502–508.